Monatshefte für Chemie - Chemical Monthly
https://doi.org/10.1007/s00706-018-2186-y

ORIGINAL PAPER

Synthesis and crystal structures of new phosphoric triamides: study of intermolecular interactions by semi-empirical calculations and Hirshfeld surface analysis

Atekeh Tarahhomi[1] · **Arie van der Lee**[2]

Received: 23 January 2018 / Accepted: 14 March 2018
© Springer-Verlag GmbH Austria, part of Springer Nature 2018

Abstract

In the present paper, crystal structures and Hirshfeld surface analyses of two new phosphoric triamides [2,3,6-F_3–C_6H_2-C(O)NH]P(O)$(X)_2$ (X=N$(CH_3)C_6H_{11}$ and N$(C_2H_5)_2$) and an improved model of $[OH_8C_4N]_3P(O)$ are investigated. Moreover, the semi-classical density sums (PIXEL) method, which enables the calculation of interaction energies for molecule–molecule pairs, and AIM calculations were used to evaluate intermolecular forces in the studied compounds. The previously reported structure [2,6-F_2-C_6H_3C(O)NH]P(O)$[NHC(CH_3)_3]_2$ with a $[C(O)NH]P(O)[NH(C)]_2$ segment, which is different than the $[C(O)NH]P(O)[N(C)(C)]_2$ segment in structures [2,3,6-F_3–C_6H_2C(O)NH]P(O)$(X)_2$, is compared to those of the newly determined structures. The Hirshfeld surface method shows that the crystal cohesions of structures [2,3,6-F_3–C_6H_2C(O)NH]P(O)$(X)_2$ are established via H···H, O···H/H···O, C···H/H···C, and F···H/H···F contacts, while for $[OH_8C_4N]_3P(O)$, H···H and O···H/H···O are the dominant contacts. From PIXEL and AIM calculations and the decomposition of the interaction energies for different molecular pairs, it is shown that the donor and acceptor capability of the atoms involved in an interaction introduces the nature and strength of that interaction. The more acidic N_{CP}–H unit in the C(O)NHP(O) segment (compared to the N_P–H unit in the $P(O)[NH(C)]_2$ segment) and the higher H-atom acceptor group P=O (compared to C=O) in the studied structures form the strongest N_{CP}–H···O=P intermolecular hydrogen bond.

Graphical abstract

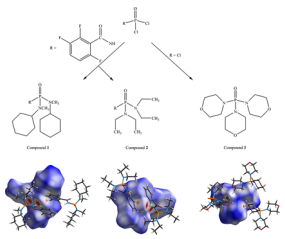

Keywords Phosphoric triamide · Crystal structure · Semi-empirical calculation · Hirshfeld surface analysis · N–H···O hydrogen bond

Electronic supplementary material The online version of this article (https://doi.org/10.1007/s00706-018-2186-y) contains supplementary material, which is available to authorized users.

✉ Atekeh Tarahhomi
tarahhomi.at@semnan.ac.ir

[1] Department of Chemistry, Semnan University, Semnan 35131-19111, Iran

[2] Institut Européen des Membranes, IEM – UMR 5635, ENSCM, CNRS, Université de Montpellier, 34095 Montpellier, France

Introduction

The preparation of phosphoramides with the segment (O=)P–N such as phosphoric triamides and their crystal growth have attracted attention because of their various potential applications such as anticancer agents [1, 2], pro-drugs [3, 4], urease inhibitors [5, 6], and chiral Brønsted acid catalysts [7, 8]. Structural analysis and modeling techniques have been used to study these phosphoramides [5, 9].

Published online: 04 July 2018

Single-crystal X-ray diffractometry is the appropriate method of choice for structural analysis. However, in this method, hydrogen atoms cannot be located with accuracy using X-rays when heavy elements are present. The exact location of hydrogen atoms is, however, crucial for the study of interaction energies in the fields of crystal engineering and materials science [10]. A new refinement technique called Hirshfeld Atom Refinement (HAR) [11] was introduced for locating hydrogen atoms more accurately. It uses aspherical atomic electron densities extracting from a crystal-field-embedded quantum-chemical electron density using Hirshfeld's scheme [12].

Once the correct structural model has been established by either classical or HAR refinements, the interactions present in the 3D structure can be analyzed by different techniques. The Hirshfeld surface analysis [13] is a useful and powerful protocol for obtaining information on trends in crystal packing and offers a considerable potential in crystal engineering. This unique approach is completed with the analysis of the associated fingerprint plots [14] which provide insight about close contacts, more distant contacts, and areas the positions where the interactions are weakest.

Another interesting analysis technique for the strength and nature of intermolecular interactions [15, 16] is based on the calculation of lattice and interaction energies of molecular pairs by the semi-classical PIXEL method [17]. This procedure which enables partitioning of the total energy into electrostatic, polarization, dispersion, and repulsion components is of such computational calculations to evaluate the importance of non-covalent interactions in the crystal packing.

The present paper is a discussion of the structural features of two new phosphoric triamides [2,3,6-F_3–C_6H_2-C(O)NH]P(O)$(X)_2$ (X=$N(CH_3)C_6H_{11}$ (**1**) and $N(C_2H_5)_2$ (**2**), Scheme 1) along with evaluation of intermolecular interactions especially the N–H···O hydrogen bonds in C(O)NHP(O)-based phosphoric triamides using the calculation of the lattice energy and intermolecular interaction energies by the PIXEL method. The previously reported structure [2,6-F_2-C_6H_3C(O)NH]P(O)$[NHC(CH_3)_3]_2$ [18] with the N_P–H···O=C hydrogen bonds (N_P–H is the NH unit of the segment P(O)$[NH(C)]_2$) in the crystal structure, where such hydrogen bonds (HBs) are not found in HB patterns of **1** and **2**, is analyzed as well by the PIXEL method. Besides, AIM (Atom In Molecule) analysis is performed on HB-dimers of **1**, **2** (both with $R_2^2(8)$ ring motif) and [2,6-F_2-C_6H_3C(O)NH]P(O)$[NHC(CH_3)_3]_2$ (forming two consecutive dimers, one with an $R_2^2(8)$ ring motif and another with an $R_2^2(12)/R_2^1(6)$ motif). An improved model of $[OH_8C_4N]_3P(O)$ (**3**) [19] (Scheme 1) is also reported. Hydrogen atoms in structures **1** and **2** are located very accurately using Hirshfeld Atom Refinement (HAR) in X-ray diffraction, where, for **3**, HAR cannot be used due to disorder in the structure. Furthermore, we have employed Hirshfeld surface analysis for the three structures **1**, **2**, and **3** which provide a convenient means of visualizing and quantifying the intermolecular interactions within the crystal structures.

Results and discussion

X-ray crystallography

The molecular structures of **1**–**3** are shown in Figs. 1, 2, and 3. The asymmetric unit of **1** and **3** consists of one molecule, whereas, for **2**, it consists of two symmetry-independent molecules. Details of crystal data and structure refinement have been provided in Table 1. Selected bond distances, angles, and torsion angles are summarized in Table 2. The structure **3** is an improved model of the previously reported structure $[OH_8C_4N]_3P(O)$ (CSD refcode BIVYAG [19]) which crystallizes in the monoclinic centrosymmetric space group $P2_1/n$.

In all compounds, the P atom displays a distorted tetrahedral environment and the P=O bond lengths are standard to the related phosphoric triamide compounds [20, 21]. In compounds **1** and **2** with a $[C(O)NH]P(O)[N(C)(C)]_2$ segment, the phosphoryl and carbonyl groups adopt an anti-orientation with respect to one another. In each of the structures, the P–N_{CP} bond distance (N_{CP} is the N atom of the segment C(O)NH-P(O)) is significantly longer than the two other P–N_P bond distances, as resulting from the electronic effect caused by the C(O) group, and the C–N–C angles are significantly smaller than the two related P–N–C angles. The bond angle sums at the tertiary nitrogen atoms of *N*-methylcyclohexylamido group in **1** and diethylamido in **2**, i.e., ∠P–N–C + ∠C–N–C + ∠C–N–P, confirm the sp^2 character of the quoted N atoms, for example 357.09(9)° and 358.41(8)° in the case of the *N*-methylcyclohexylamido group in **1**. Such N atoms do not take part in hydrogen bonding as an acceptor, because they have a low Lewis-base character.

The hydrogen-bond patterns for structures **1** and **2** are similar, where the *anti*-orientation of P=O and C=O groups relative to one another results in a centrosymmetric (**1**) or non-centrosymmetric (**2**) dimer via the N_{CP}–H···O=P hydrogen bonds forming $R_2^2(8)$ ring motif. In addition to the N–H···O hydrogen bonds, the structure of **1** is stabilized to a lesser extent by the weak cohesion from the C–H···O and π···π stacking interactions (Table 3). These interactions lead to the formation of a 2D layer parallel to *ac* plane composed of H-bonded dimers (Fig. 4). In the crystal

Scheme 1

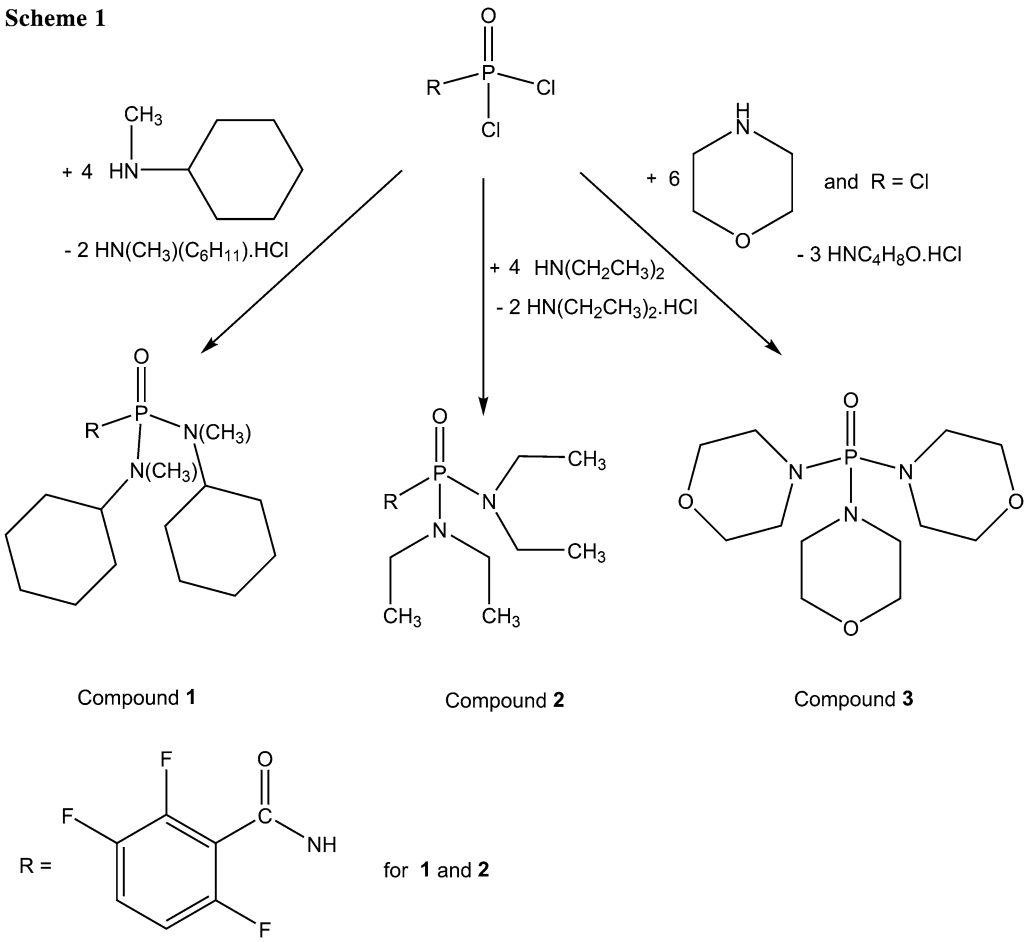

structure of **2**, the non-centrosymmetric dimers are connected through the C–H···O, π···π stacking and H···H interactions (Table 3) leading to a 2D layer parallel to (111) plane (Fig. 5).

Structure **3** does not have any N–H···O strong hydrogen bonds resulting from the absence of any N–H units. The crystal stabilization is produced via C–H···O interactions (Table 3) which extend the structure to a three-dimensional network.

Evaluation of N–H…O hydrogen bonds by intermolecular interaction energies and topological properties

The lattice energies of **1**–**3** and the previously reported structure [2,6-F_2-C_6H_3C(O)NH]P(O)[$NHC(CH_3)_3$]$_2$ ([C(O)NH]P(O)[*tert*-Bu]$_2$) calculated using the PIXEL method are presented in Table 4. Energy partitioning shows that, for all compounds, the major contributions towards the lattice stabilization originate from the coulombic and dispersion components, while the remaining contribution is afforded by the polarization energy.

A simple review of the lattice energies reported in Table 4 imparts that the highest values are found for phosphoric triamides **1** and **2** with the segment [C(O)NH]P(O)[N(C)(C)]$_2$, then, [C(O)NH]P(O)[*tert*-Bu]$_2$ with the segment [C(O)NH]P(O)[NH(C)]$_2$ and eventually, **3** with the segment P(O)[N(C)(C)]$_3$. This is an expected result as the crystal cohesions of **1** and **2** are stabilized by the strong N_{CP}–H···O=P hydrogen bonds, while, for [C(O)NH]P(O)[*tert*-Bu]$_2$, the slightly weaker N–H···O (N_P–H···O=C and N_{CP}–H···O=P) hydrogen bonds relative to N_{CP}–H···O=P in **1** and **2** are involved in crystal packing. Finally, in the crystal structure of **3**, there is no strong hydrogen bond. In this way, the results of lattice energy calculations confirm the obtained findings of the statistical analysis on the strength of N–H···O hydrogen bonds in phosphoric triamides [22, 23].

To further evaluate the N–H···O hydrogen bonds, different intermolecular interactions in **1**–**3** and [C(O)NH]-P(O)[*tert*-Bu]$_2$ along with geometrical parameters, symmetry, and interaction energies partitioned into different energy components are presented in Table 5. The molecular pairs involved in the crystal packing of **1**–**3** and

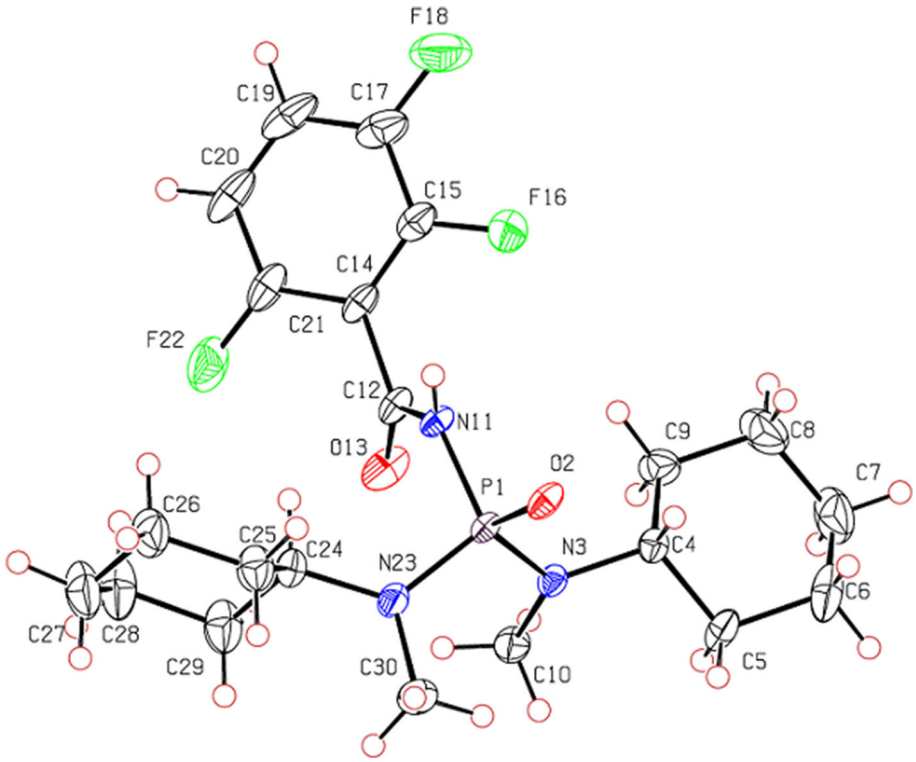

Fig. 1 ORTEP-style plot and atom-labeling scheme for structure **1**. Displacement ellipsoids are drawn at the 50% probability level and H atoms are drawn as circles of arbitrary radii

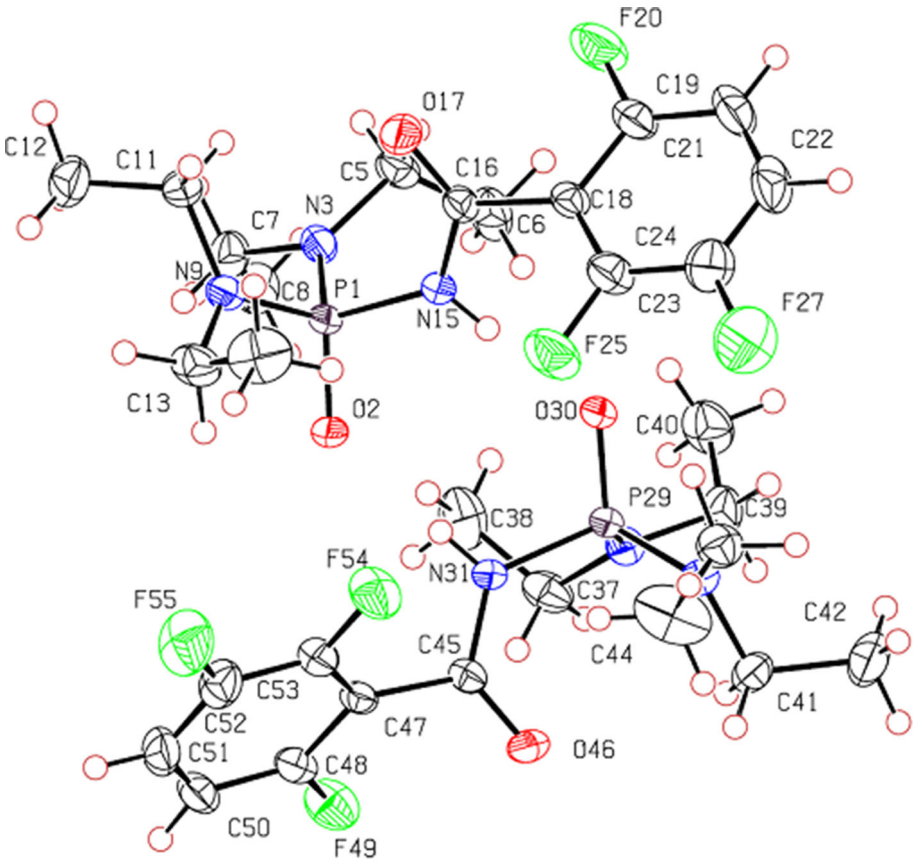

Fig. 2 ORTEP-style plot and atom-labeling scheme for structure **2**, showing two independent molecules P1 and P29. Displacement ellipsoids are drawn at the 50% probability level and H atoms are drawn as circles of arbitrary radii

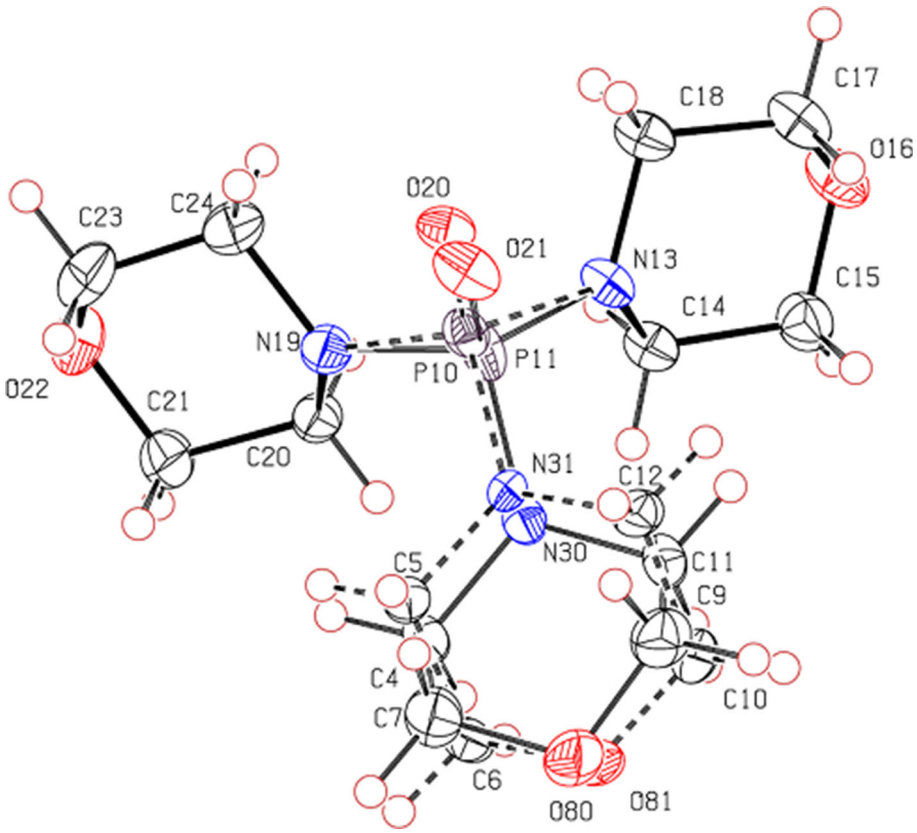

Fig. 3 ORTEP-style plot and atom-labeling scheme for structure **3**. Displacement ellipsoids are drawn at the 50% probability level and H atoms are drawn as circles of arbitrary radii. Bonds connecting disordered atoms with minor components are shown as dash lines

[C(O)NH]P(O)[*tert*-Bu]$_2$ and corresponding intermolecular interactions considered in interaction energies calculations are shown in Figs. 6 and 7.

In **1**, **2**, and [C(O)NH]P(O)[*tert*-Bu]$_2$, the most stable molecular pairs observed are the hydrogen-bonded dimers of N_{CP}–H···O=P having a stabilization energy of − 116.3, − 122.5, and − 96.8 kJ/mol, respectively. The stability of these molecular pairs is provided by the coulombic contribution (52% for **1** and **2**, and 47% for [C(O)NH]P(O)[*tert*-Bu]$_2$), followed by polarization (26% for **1** and **2**, and 33% for [C(O)NH]P(O)[*tert*-Bu]$_2$) and dispersion (22% for **1** and **2**, and 21% for [C(O)NH]-P(O)[*tert*-Bu]$_2$) components, respectively (Table 5). In [C(O)NH]P(O)[*tert*-Bu]$_2$, the coulombic interactions are smaller and the polarization contributions are larger than in **1** and **2**, respectively. This can be attributed to the lower strength of the N_{CP}–H…O=P hydrogen bond in [C(O)NH]P(O)[NH(C)]$_2$-based phosphoric triamides ([C(O)NH]P(O)[*tert*-Bu]$_2$) compared to that in [C(O)NH]P(O)[N(C)(C)]$_2$-based phosphoric triamides (**1** and **2**) [22, 23].

In [C(O)NH]P(O)[*tert*-Bu]$_2$, the next most stable molecular pair contains the N_P–H···O=C hydrogen bond whose interaction energy is calculated to be − 81.4 kJ/mol. In this molecular pair, the strength order of the contributions is the same as in the N_{CP}–H···O=P hydrogen bond, i.e., coulombic interactions dominate before the polarization and dispersion contributions. Other molecular pairs have weak interactions such as C–H···O and π···π interactions with energies less than − 48.0 kJ/mol (Table 5). In this way, the results show that in **1**, **2**, and [C(O)NH]P(O)[*tert*-Bu]$_2$ with at least one N–H unit, the N–H···O hydrogen bonds are the most important intermolecular interactions.

Moreover, in **1** and **2**, the N_{CP}–H···O=P hydrogen bonds contribute more to the lattice energy than the N_P–H···O=C hydrogen bonds in [C(O)NH]P(O)[*tert*-Bu]$_2$. These results are in agreement with those obtained from other reported analyses on the N–H···O hydrogen bonds in C(O)NHP(O)-based phosphoric triamides [22, 23] which show that the N_{CP}–H···O=P hydrogen bond is stronger than the N_P–H···O=C hydrogen bond.

Finally, for **3**, the most stable molecular pair (I) has an interaction energy being − 40.6 kJ/mol (Table 5), where the structure only include the C–H···O hydrogen bonds without any N–H···O interaction as a result of the lack of the N–H unit in this structure. The stability of this molecular pair is driven mainly by dispersion forces (55%), and then by coulombic (28%) and polarization (17%) contributions, respectively.

The N–H···O hydrogen bonds were also analyzed by a Quantum Theory of Atom In Molecule (QTAIM) analysis

Table 1 Crystal data and structure refinement for compounds **1**–**3**

	1	**2**	**3**
Empirical formula	$C_{21}H_{31}F_3N_3O_2P$	$C_{15}H_{23}F_3N_3O_2P$	$C_{12}H_{24}N_3O_4P$
Mr/g mol^{-1}	445.46	365.33	305.31
T/K	175	175	175
λ/Å	0.71073	0.71073	0.71073
Crystal system	Triclinic	Triclinic	Monoclinic
Space group	$P\ \bar{1}$	$P\ \bar{1}$	$P2_1/n$
a/Å	10.2200(3)	10.0500(5)	9.1334(4)
b/Å	10.6530(4)	10.4670(5)	11.1786(5)
c/Å	11.3031(5)	19.5123(10)	14.6624(6)
α/°	69.721(3)	78.668(4)	90
β/°	79.415(3)	80.643(4)	96.979(4)
γ/°	81.464(3)	63.230(5)	90
V/Å^3	1129.89(5)	1790.39(9)	1485.92(6)
Z	2	4	4
Density/g cm^{-3}	1.309	1.355	1.365
μ/mm^{-1}	0.168	0.196	0.202
F(000)	472	768	656
Crystal size/mm^3	0.10 × 0.40 × 0.50	0.35 × 0.47 × 0.55	0.22 × 0.40 × 0.45
Crystal color/habit	Colorless/thick plate	Colorless/prism	Colorless/prism
R_{int}	0.045	0.043	0.048
Q_{max}/°	32.665	29.265	29.075
Resolution/Å	0.66	0.73	0.73
N_{tot} (measured)	40,799	17,694	15,826
N_{ref} (unique)	7721	8266	3624
N_{ref} ($I > 2\sigma(I)$)	6583	6225	3023
N_{ref} (least-squares)	7716	8264	3622
N_{par}	274	433	254
$<s(I)/I>$	0.0516	0.0638	0.0596
R_1, wR_2 ($I > 2\sigma(I)$)	0.0424, 0.0909	0.0540, 0.1319	0.0501, 0.0655
R_1, wR_2 (all)	0.0528, 0.0989	0.0771, 0.1548	0.0638, 0.0700
GOF	0.9062	0.9028	0.9960
Dr/e Å^{-3}	− 0.40/0.45	− 0.47/0.63	− 0.35/0.39

using AIM2000 on dimers of **1**, **2**, and [C(O)NH]P(O)[*tert*-Bu]$_2$ for obtaining the bond critical points (BCPs) between the interacting atoms and, then, the topological parameters $\rho_{(r)}$ and $L_{(r)}$ (= $-\nabla^2\rho_{(r)}$). The dimers have a N_{CP}–H···O=P hydrogen bond inside the $R_2^2(8)$ ring motif for **1** (molecular pair I in Fig. 6, left), **2** (molecular pair I in Fig. 6, right) and [C(O)NH]P(O)[*tert*-Bu]$_2$ (molecular pair I in Fig. 7, right), and the N_P–H···O=C/$R_2^2(12)$ hydrogen bond (molecular pair II in Fig. 7, right) for [C(O)NH]P(O)[*tert*-Bu]$_2$. As can be seen in Table 6, the $\rho_{(r)}$ and $L_{(r)}$ values of H···O contacts for N_{CP}–H···O=P hydrogen bonds in **1**, **2**, and [C(O)NH]P(O)[*tert*-Bu]$_2$ are higher than those for N_P–H···O=C hydrogen bond in [C(O)NH]P(O)[*tert*-Bu]$_2$, confirming the higher strength of the H···O interaction in N_{CP}–H···O=P than in N_P–H···O=C [22, 23]. Moreover, a comparison of the $\rho_{(r)}$ and $L_{(r)}$ values of H···O contacts for N_{CP}–H···O=P hydrogen bonds shows that these values for [C(O)NH]P(O)[*tert*-Bu]$_2$ are slightly lower than those in **1** and **2**. On the basis of this observation, it is deduced that the N_{CP}–H···O=P hydrogen bond in phosphoric triamides with a segment [C(O)NH]P(O)[N(C)(C)]$_2$ (such as **1** and **2**) is slightly stronger than that in phosphoric triamides with a [C(O)NH]P(O)[NH(C)]$_2$ segment (such as [C(O)NH]P(O)[*tert*-Bu]$_2$). Finally, the results reveal that the N_{CP}–H unit and the P=O group take part in stronger N–H···O hydrogen bonds compared to the N_P–H unit and the C=O group, respectively. This demonstrates the more acidic character of the proton in N_{CP}–H compared to that in N_P–H due to the resonance interaction of N_{CP} lone pair with the C=O bond and the higher H-atom acceptor capability of $O_{P=O}$ compared to $O_{C=O}$.

Table 2 Selected bond distances (Å) and angles (°) for compound **1**–**3**

Compound **1**					
P1–O2	1.4860(8)	N3–P1–O2	110.60(5)	N11–P1–N23	105.76(5)
P1–N3	1.6322(9)	N11–P1–O2	105.22(5)	O13–C12–N11–P1	2.4(2)
P1–N11	1.6886(9)	N23–P1–O2	117.11(6)	O2–P1–N11–C12	164.0(1)
P1–N23	1.6331(11)	N3–P1–N11	112.59(5)	N3–P1–N11–C12	43.5(1)
C12–O13	1.2148(14)	N3–P1–N23	105.64(5)	N23–P1–N11–C12	− 71.4(1)
Compound **2**					
P1–O2	1.4822(17)	N3–P1–O2	116.87(12)	N31–P29–N36	104.85(11)
P29–O30	1.4821(18)	N9–P1–O2	109.74(11)	N33–P29–N36	107.49(12)
P1–N3	1.628(2)	N15–P1–O2	106.02(10)	O17–C16–N15–P1	− 2.4(4)
P1–N9	1.632(2)	N3–P1–N9	106.80(12)	O2–P1–N15–C16	− 159.6(2)
P1–N15	1.688(2)	N3–P1–N15	104.24(11)	N3–P1–N15–C16	76.5(3)
P29–N31	1.696(2)	N9–P1–N15	113.25(11)	N9–P1–N15–C16	− 39.2(3)
P29–N33	1.634(2)	N31–P29–O30	105.41(10)	O46–C45–N31–P29	− 7.2(4)
P29–N36	1.628(2)	N33–P29–O30	109.85(11)	O30–P29–N31–C45	− 158.6(2)
C16–O17	1.212(3)	N36–P29–O30	117.01(12)	N33–P29–N31–C45	− 39.1(3)
C45–O46	1.213(3)	N31–P29–N33	112.23(11)	N36–P29–N31–C45	77.3(2)
Compound **3**					
P11–O21	1.480(10)	N20–P10–O31	121.1(7)	N13–P10–N31	100.3(7)
P10–O20	1.488(11)	N13–P11–O21	109.5(6)	N19–P10–N31	103.0(7)
P11–N30	1.694(12)	N19–P11–O21	108.7(7)	O21–P11–N13–C18	− 30.2(7)
P10–N31	1.602(13)	N13–P11–N19	113.5(5)	O21–P11–N19–C24	35.6(7)
P11–N13	1.617(10)	N13–P11–N30	103.4(6)	O21–P11–N30–C4	92.0(1)
P11–N19	1.709(9)	N19–P11–N30	103.5(6)	O20–P10–N31–C5	85.0(1)
N30–P11–O21	118.2(6)	N13–P10–N19	113.2(6)		

Study of intermolecular interactions by Hirshfeld surface analysis

The Hirshfeld surfaces (HSs) of **1**, molecules P1 and P29 of **2**, and **3** mapped over the d_{norm} range of − 0.18 to 1.61 Å are shown in Figs. 8, 9, 10, 11, and 12 and S1–S3. HSs mapped over the shape index for **1** and molecules P1 and P29 of **2** are given in Figs. 9, 11, and S2. For **3** that shows disorder in the P=O group and one of morpholine rings, the HSs were separately generated for both possible major (Fig. 12) and minor (Fig. S3) components. The interaction proportions for the two models are nearly the same having a variability of less than 0.5%; hence, for the following discussion, the major component in **3** is discussed only and is treated as fully occupied.

For **1** and both molecules of **2**, the dominant interactions between the N–H unit and phosphoryl O atom (Table 3) can be seen in the corresponding HSs as the deep red spots shown in Figs. 8, 10, and S1. In these HSs, the light red spots are due to C–H···O=P interactions (Table 3). In **1**, other visible spots on the HS are the small pale red spots which correspond to C–H···O=C contacts (Table 3), reflecting the smaller H-atom acceptor capability of C=O relative to P=O. In Figs. 9, 11, and S2, the C–H···F hydrogen bonds (black dash lines) can be recognized as white areas to which show that such interactions are rather weak.

In the HS of **3** (Fig. 12), the C–H···O hydrogen bonds from the interactions between the O atoms (of P=O group or NC_4H_8O rings) and CH groups (of NC_4H_8O rings) (Table 3) appear as red areas. No other characteristic contacts as red spots are seen on the HS.

Figures 8, 9, 10, 11, 12, S1–S3 also show the FPs of **1**–**3**. These plots are the graphical views with the d_e and d_i distance scales which analyze the intermolecular contacts and their contributions to the corresponding total HS at the same time.

An important feature of the FPs is that they are rather symmetric for **1** and **3**, while they have slightly asymmetrical shapes especially in the upper areas of the plots for two independent molecules of **2**. This highlights the isotropic environment of molecules in the solid state of **1** and **3** [24], whereas two molecules P1 and P29 present in crystal **2** are involved in slightly different intermolecular interaction patterns.

The FPs reveal that the main intermolecular interactions in **1**–**3** are H···H contacts which are a common feature of phosphoric triamide molecular crystals [20] and cover most of the area in the plots with the most significant contribution to the total HSs (57.4% for **1**, 48.1% for molecule P1

Table 3 Hydrogen bonds and short contacts' geometries (Å, °) for compounds **1**–**3**

D–H…*A*	*d*(*D*–H)	*d*(H…*A*)	*d*(*D*…A)	∠(*D*H*A*)
Compound **1**				
N11–H111···O2^{i}	0.858	1.894	2.736(2)	166.5
C9–H92···O13^{ii}	0.986	2.535	3.465(2)	157.2
C10–H101···O13^{ii}	0.972	2.607	3.511(2)	154.9
C20–H201···O2^{iii}	0.944	2.375	3.138(2)	137.7
Cg…Cg*	–	–	3.6854(1)	–
Compound **2**				
N15–H151···O30	0.832	1.928	2.749(5)	168.6
N31–H311···O2	0.848	1.940	2.779(5)	169.7
C50–H501···O2^{i}	0.920	2.412	3.251(3)	151.7
C21–H211···O30^{ii}	0.922	2.484	3.213(4)	136.2
C11–H112···H371–C37^{iii}	–	2.3477	–	–
Cg…Cg†	–	–	4.0260(2)	–
Cg…Cg‡	–	–	4.0666(2)	–
Compound **3**				
C20–H201···O21^{i}	0.955	2.318	3.134(8)	143.0
C11–H112···O22^{ii}	0.958	2.467	3.352(4)	153.5
C17–H171···O22^{ii}	0.958	2.702	3.605(2)	157.3
C14–H142···O80^{iii}	0.959	2.642	3.580(5)	166.0
C20–H202···O80^{iii}	0.968	2.673	3.630(5)	170.3
C4–H42···O16^{iv}	0.962	2.600	3.291(5)	128.9

Symmetry transformations used to generate equivalent atoms for **1**: (i): $-x+1, -y+2, -z$; (ii): $-x+1, -y+2, -z+1$; (iii): $x-1, y, z$; for **2**: (i): $-x+1, -y+2, -z+1$; (ii): $-x+1, -y+1, -z+2$; (iii): $x-1, y+1, z$; for **3**: (i): $-x+\frac{3}{2}, y+\frac{1}{2}, -z+\frac{3}{2}$; (ii) $x-1, y, z$; (iii) $x+\frac{1}{2}, -y+\frac{1}{2}, z+\frac{1}{2}$; (iv): $x+\frac{1}{2}, -y+\frac{1}{2}, z-\frac{1}{2}$

*Cg = centroid of the phenyl ring of molecule **1**

†Cg = centroid of the phenyl ring of molecule P29 of **2**

‡Cg = centroid of the phenyl ring of molecule P1 of **2**

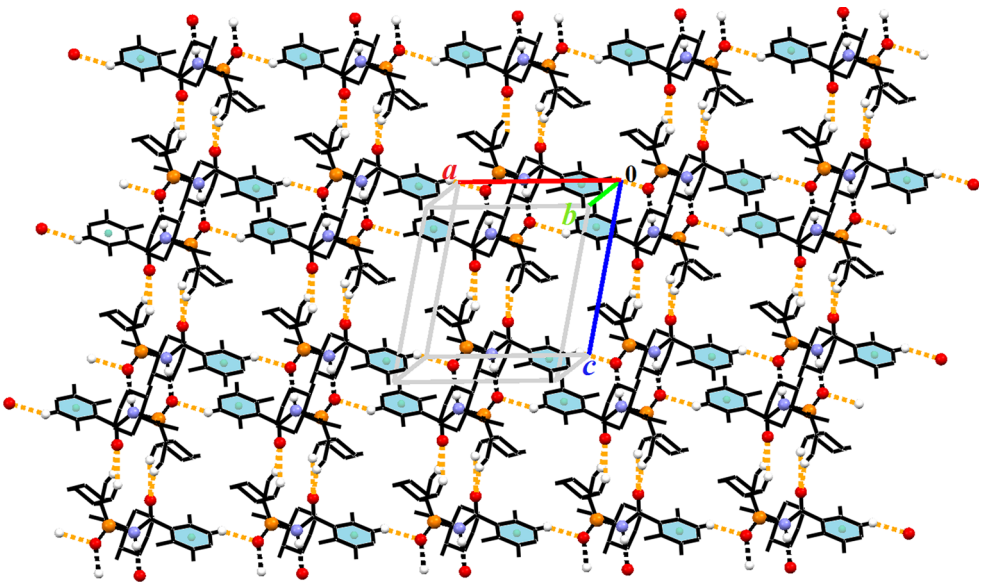

Fig. 4 Partial crystal packing diagram for **1** is shown. 2D layer parallel to *ac* plane is formed via C–H…O (orange dashed lines) and π…π stacking interactions (Table 3) connecting the centrosymmetric N–H…O=P dimers (black dashed lines). H, P, O, and N atoms involved in N–H…O contacts are shown as "small balls" and the other H atoms bonded to C atoms have been omitted for clarity

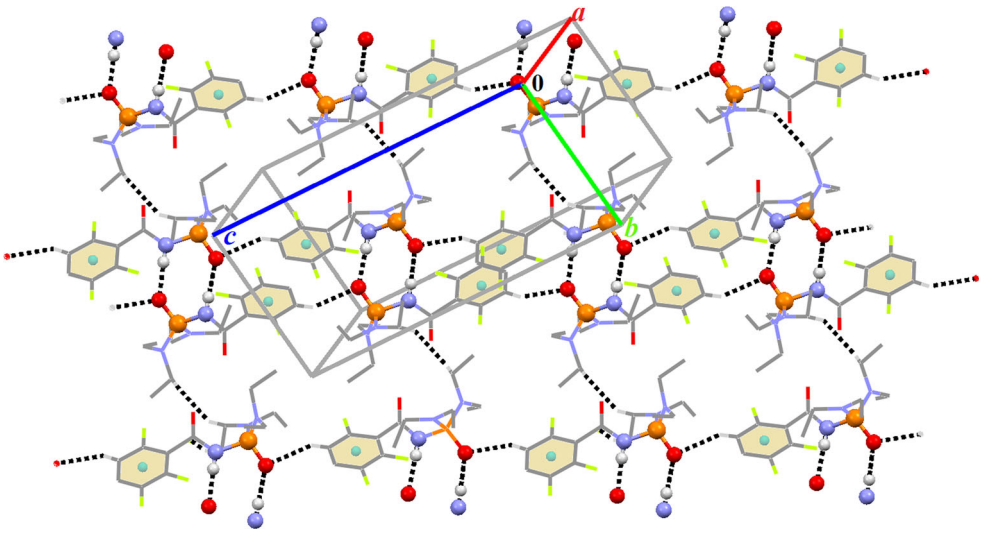

Fig. 5 Part of the crystal packing of structure **2**, adjacent molecules are linked via the H…O and H…H interactions (black dashed lines), and π…π stacking (Table 3) composed of H-bonded dimers, forming a 2D layer parallel to (111) plane. H, P, O, and N atoms involved in N–H…O contacts are shown as "small balls" and the other H atoms bonded to C atoms have been omitted for clarity

Table 4 Lattice energies of compounds **1–3** and [C(O)NH]P(O)[*tert*-Bu]$_2$ partitioned into different energy components

Compound	E_{coul}/ kJ mol^{-1}	E_{pol}/ kJ mol^{-1}	E_{disp}/ kJ mol^{-1}	E_{rep}/ kJ mol^{-1}	E_{tot}/ kJ mol^{-1}
1	− 112.8	− 48.7	− 183.1	177.5	− 167.1
2	− 103.3	− 44.2	− 150.6	141.0	− 157.2
3	− 79.4	− 35.8	− 154.1	143.9	− 125.4
[C(O)NH]P(O)[*tert*-Bu]$_2$	− 102.6	− 41.9	− 143.4	132.5	− 155.4

of **2**, 44.4% for molecule P29 of **2**, and 72.8% for **3**). These contacts provide the closest interactions with $d_i + d_e > 2.3$ Å for **1**, 2.2 Å for both molecules P1 and P29 of **2**, and 2.1 Å for **3**, showing a short broad (**1** and **3**) or thin (both P1 and P29 of **2**) spike on the plot diagonal.

In the decomposed H···H FPs, the other important point is the color change from blue to green in the region of 1.2 Å $< d_e$, $d_i < 1.8$ Å for **1** and P29 of **2**, 1.1 Å $< d_e$, $d_i < 1.6$ Å for P1 of **2**, and 1.4 Å $< d_e$, $d_i < 1.9$ Å for **3**, which show that the occurrence frequency of H···H contacts is increased in the mentioned regions.

For **1** and **2**, prominent pairs of sharp spikes with almost equal lengths in the region 1.7 Å $< d_e + d_i < 2.6$ Å of the FPs (Figs. 8, 10, and S1) are characteristics of O···H/H···O contacts made from the N–H···O=P, C–H···O=P, and C–H···O=C hydrogen bonds. These O···H/H···O contacts comprise a 10.6% (**1**) and a 13.4% (P1 and P29 of **2**) contribution to the corresponding HSs. As can be deduced from the figures, the upper spike corresponds to the donor spike (H atoms from N–H or C–H interacting with O atoms of P=O or C=O groups), with the lower spike being an acceptor spike (O atoms from P=O or C=O groups interacting with the H atoms of N–H or C–H).

For **3**, the C–H···O intermolecular interactions (O···H/H···O contacts, 27.0%) appear as three pair moderate distinct spikes in the 2D FP (Fig. 12): the close (in the region 2.2 Å $< d_e + d_i < 2.8$ Å), middle (2.1 Å $< d_e + d_i < 2.7$ Å), and far (2.3 Å $< d_e + d_i < 2.8$ Å) double spikes to the plot diagonal. The middle ones with the closest contact near 2.1 Å which are longer than the other two pair spikes (the close and far ones) are probable resulting from the C–H···O=P hydrogen bonds, where the O atom of P=O is a better H-bond acceptor than the O atom of the NC_4H_8O rings.

The points in the (d_e, d_i) regions of the top left (1.7–2.6 Å, 1.2–2.0 Å, $d_e > d_i$) and the bottom right (1.2–2.2 Å, 1.7–2.7 Å, $d_e < d_i$) in the FP of **1** are due to C···H/H···C interactions (Fig. 8), having a 7.3% contribution to the total interactions. For **2**, similar regions on the FPs appearing as wings are found for C···H/H···C contacts (Figs. 10 and S1), 10.9% contribution [top left (1.7–2.5, 1.1–2.0 Å) and bottom right (1.1–2.4, 1.7–2.8 Å] for molecule P1 and 9.5% [(1.7–2.7, 1.1–2.2 Å) and (1.1–2.0, 1.7–2.5 Å)] for P29.

For **1** and **2**, the F···H/H···F contacts (21.7% for **1**, 25.1% for P1 of **2,** and 30.1% for P29 of **2**) show up in the upward middle of scattered points in the corresponding plots. For **1**, the mentioned area contains two symmetric broad spikes at left and right bottom sections of the plot with minimum $d_e + d_i$ values of 2.6 Å, whereas these spikes become very short or thin in F···H/H···F FPs of molecules P1 and P29 of **2**.

The C···C FP of **1** (1.4% contribution, in the region 1.6 Å $< d_e$, $d_i < 2.1$ Å) and molecules P1 (1.2%, 1.7 Å $< d_e$, $d_i < 2.2$ Å) and P29 (1.3%, 1.7 Å $< d_e$, $d_i < 2.1$ Å) of **2** in Figs. 9, 11, and S2 show the

Table 5 List of intermolecular interaction energies (kJ/mol) for short contacts of **1–3** and [C(O)NH]P(O)[*tert*-Bu]$_2$

Molecular pairs	Interactions	Symmetry code	X…A/Å	D–X…A/°	Centroid…Centroid Distance/Å	E_{coul}	E_{pol}	E_{disp}	E_{rep}	E_{tot}
Compound **1**										
I	N11–H111···O2	$-x+1, -y+2, -z$	1.894	166.5	5.234	− 133.8	− 56.1	− 66.8	140.3	− 116.3
II	C9–H92···O13	$-x+1, -y+2, -z+1$	2.535	157.2	6.574	− 19.6	− 9.6	− 56.3	38.2	− 47.3
II	C10–H101···O13	$-x+1, -y+2, -z+1$	2.607	154.9	6.574	− 19.6	− 9.6	− 56.3	38.2	− 47.3
III	C20–H201···O2	$x-1, y, z$	2.375	137.7	10.220	− 24.5	− 9.8	− 28.9	28.0	− 35.3
IV	C19…C21 (π…π)	$-x+2, -y+2, -z$	3.685	–	9.198	− 0.6	− 5.4	− 44.3	31.4	− 18.9
Compound **2**										
I	N15–H151···O30	x, y, z	1.928	168.6	4.979	− 133.9	− 57.4	− 65.9	134.8	− 122.5
I	N31–H311···O2	x, y, z	1.940	169.7	4.979	− 133.9	− 57.4	− 65.9	134.8	− 122.5
II	C21–H211···O30	$-x+1, -y+1, -z+2$	2.484	136.2	10.010	− 22.4	− 9.2	− 26.7	24.6	− 33.8
III	C11–H112···H371–C37	$x+1, y-1, z$	2.3477	–	6.439	− 10.1	− 6.3	− 43.1	26.9	− 32.6
IV	C50–H501···O2	$-x+1, -y+2, -z+1$	2.412	151.7	10.270	− 20.8	− 7.2	− 16.7	16.5	− 28.2
V	C48…C51 (π…π)	$-x+1, -y+2, -z+1$	4.026	–	8.918	0.1	− 3.5	− 30.9	19.4	− 14.9
VI	C19…C22 (π…π)	$-x+1, -y+1, -z+2$	4.067	–	9.036	0.7	− 3.7	− 27.9	16.8	− 14.0
VII	C38–H381···F55	$x-1, y, z$	2.663	138.7	10.066	− 1.4	− 0.7	− 9.6	3.7	− 7.9
Compound **3**										
I	C20–H201···O21	$-x+\frac{3}{2}, y-\frac{1}{2}, -z+\frac{3}{2}$	2.318	143.0	5.790	− 21.2	− 12.3	− 41.1	34.0	− 40.6
II	C14–H142···O80	$x-\frac{1}{2}, -y+\frac{1}{2}, z-\frac{1}{2}$	2.642	166.0	8.370	− 13.5	− 4.4	− 22.7	15.1	− 25.4
II	C20–H202···O80	$x+\frac{1}{2}, -y+\frac{1}{2}, z+\frac{1}{2},$	2.673	170.3	8.370	− 13.5	− 4.4	− 22.7	15.1	− 25.4
III	C11–H112···O22	$x-1, y, z$	2.467	153.5	9.133	− 10.5	− 4.8	− 22.2	18.9	− 18.6
III	C17–H171···O22	$x-1, y, z$	2.702	157.3	9.133	− 10.5	− 4.8	− 22.2	18.9	− 18.6
IV	C4–H42···O16	$x-\frac{1}{2}, -y+\frac{1}{2}, z+\frac{1}{2}$	2.600	128.9	9.291	− 7.6	− 3.6	− 22.2	17.3	− 16.1
[C(O)NH]P(O)[*tert*-Bu]$_2$										
I	N1–H1 N···O2	$-x, -y+1, -z+1$	1.96(1)	172(2)	4.807	− 99.7	− 44.2	− 69.5	116.5	− 96.8
I	C5···O2	$-x, -y+1, -z+1$	3.179(3)	–	4.807	− 99.7	− 44.2	− 69.5	116.5	− 96.8
II	N2–H2 N···O1	$-x+1, -y+1, -z+1$	2.22(1)	160(2)	5.322	− 71.8	− 26.0	− 57.6	74.1	− 81.4
II	N3–H3 N···O1	$-x+1, -y+1, -z+1$	2.22(2)	152(2)	5.322	− 71.8	− 26.0	− 57.6	74.1	− 81.4

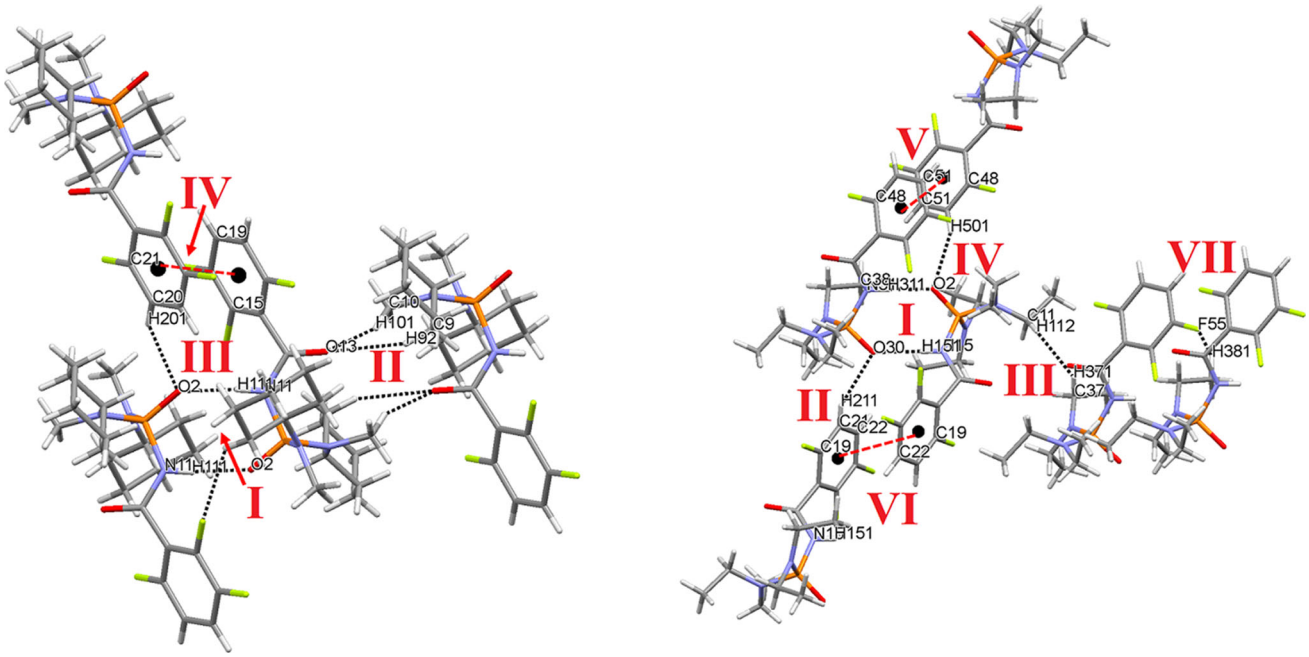

Fig. 6 View of crystal packing of **1** (left) and **2** (right) showing molecular pairs and corresponding intermolecular interactions considered in interaction energies calculations

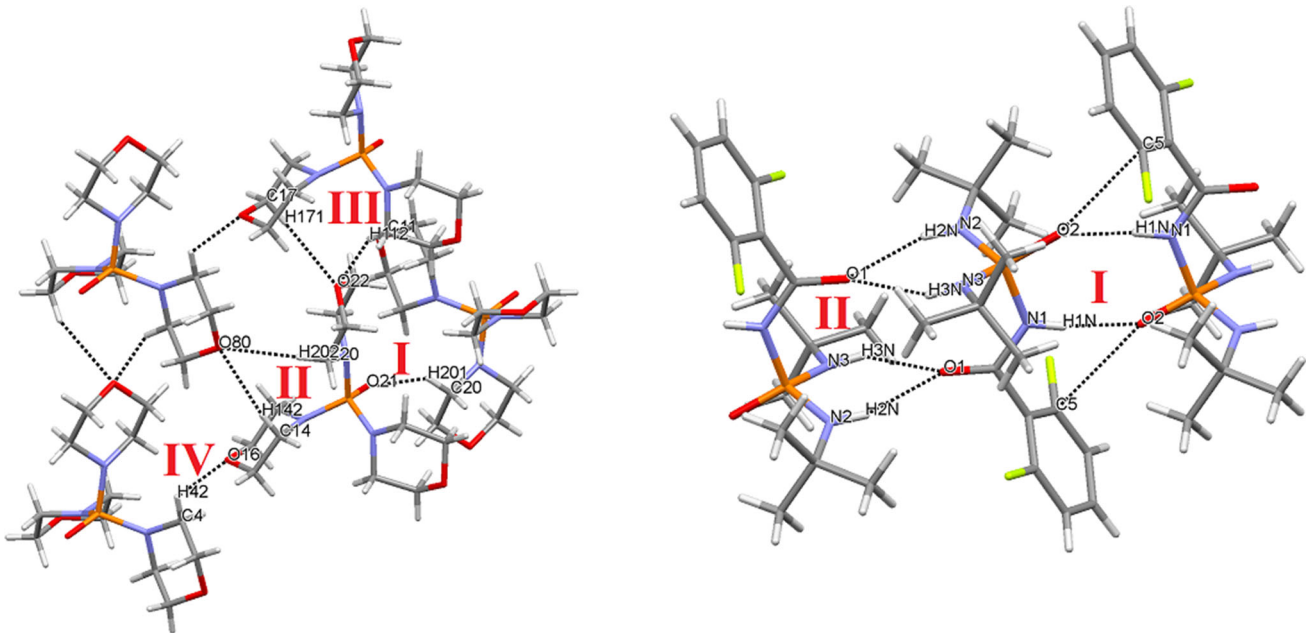

Fig. 7 View of crystal packing of **3** (left) and [C(O)NH]P(O)[*tert*-Bu]$_2$ (right) showing molecular pairs and corresponding intermolecular interactions considered in interaction energies calculations

characteristic motifs defined as a stacking kite on the middle plot due to the presence of C···C interactions between unsaturated C atoms such as π···π interactions. These interactions are also reflected by red–blue triangles on the shape index surfaces of **1** and molecules P1 and P29 of **2** in Figs. 9, 11, and S2. Where HS mapped with the shape index, as a feature of HS analysis allowing for the identification of complementarity between molecules in the crystal packing structure, can be used to identify characteristic packing modes, in particular planar stacking arrangements and the presence of aromatic stacking interactions such as C–H···π and π···π interactions [25].

Table 6 N–H…O hydrogen bonds (Å) and topological properties (in a.u.) for the atoms involved in the hydrogen bonds for compounds **1**, **2**, and [C(O)NH]P(O)[*tert*-Bu]$_2$, calculated at the MP2/6-31G(d,p)

Compound/graph set type of hydrogen bond	$d(D\ldots A)$/Å experimental	$\rho_{(r)}/L_{(r)}$ at the BCP/a.u. H…O
1/ $R_2^2(8)$		
N_{CP}–H…O(P)	2.736(2)	0.027/− 0.027
2/ $R_2^2(8)$		
N_{CP}–H…O(P)	2.749(5)	0.024/− 0.023
N_{CP}–H…O(P)	2.779(5)	0.025/− 0.025
[C(O)NH]P(O)[*tert*-Bu]$_2$/$R_2^2(8)$/$R_2^2(12)$		
N_{CP}–H…O(P)	2.808(2)	0.023/− 0.022
N_P–H…O(C)	3.042(2)	0.012/− 0.012
N_P–H…O(C)	3.008(2)	0.013/− 0.013

The average values is reported

Conclusions

X-ray crystallography study, Hirshfeld surface (HS) analysis, and semi-empirical calculation using the PIXEL method for two new C(O)NHP(O)-based phosphoric triamides (**1** and **2**) and an improved model of $[OH_8C_4N]_3$-P(O) (**3**) were presented here. Moreover, a previously reported structure [2,6-F_2-C_6H_3C(O)NH]P(O)[NHC$(CH_3)_3]_2$ was modeled for PIXEL and AIM calculations beside structures **1** and **2**. The main features from these investigations are: (a) the HS analysis results show that the molecular interactions in **1** and **2** are dominated by H···H and F···H/H···F interactions (non-red areas on HSs) which together account for 73–80% of the HS. Whereas the contribution of the O···H/H···O, appeared as red spots and C···H/H···C contacts altogether, is less than 25%. For **3**, especially H···H and O···H/H···O contacts (red spots on the HS) contribute to the crystal cohesion; (b) from PIXEL

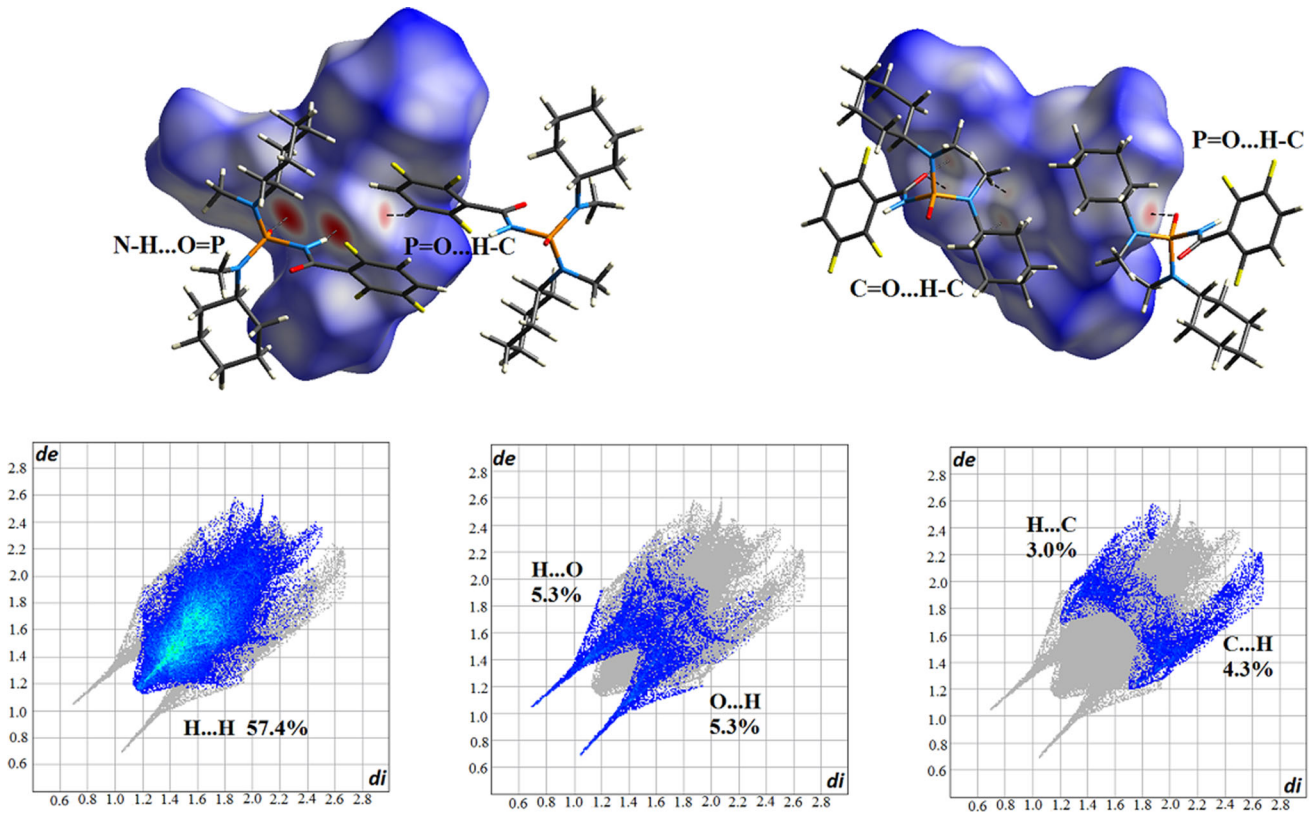

Fig. 8 Up: d_{norm} Hirshfeld surface surrounded by neighboring molecules associated with close contacts for **1** in two different orientations. Down: decomposed fingerprint plots and percentage contributions to the total HS for intermolecular contacts H…H, O…H/H…O, and C…H/H…C for **1**. The full fingerprint plot appears as a grey shadow below each decomposed plot

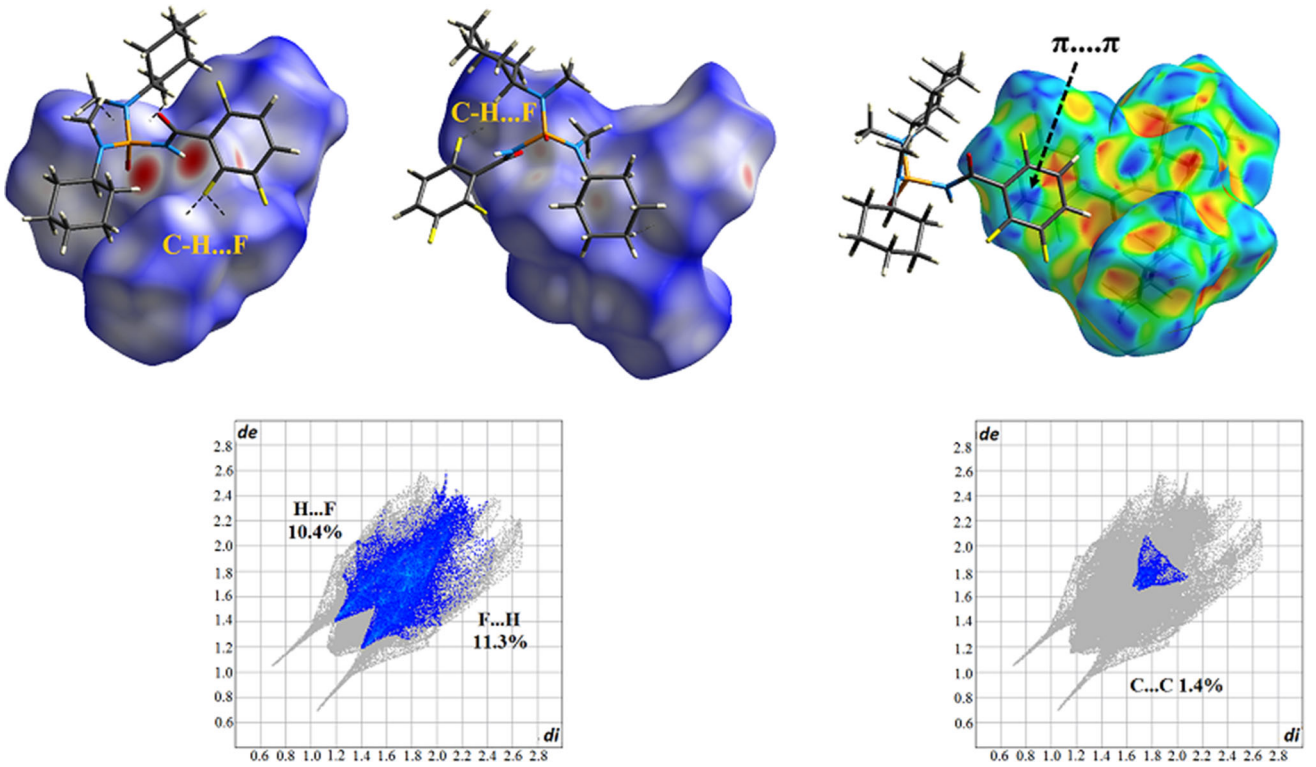

Fig. 9 Up: d_{norm} Hirshfeld surface in two different orientations (left and middle) and Hirshfeld surface mapped with shape index (right), surrounded by neighboring molecules associated with close contacts H…F/F…H (black dash lines, white areas) or π…π stacking, for **1**. Down: decomposed fingerprint plots and percentage contributions to the total HS for intermolecular contacts F…H/H…F and C…C for **1**. The full fingerprint plot appears as a grey shadow below each decomposed plot

calculations, it is revealed that coulombic contribution plays a dominating role in the lattice energy for strong hydrogen bonds N_{CP}–H···O=P and N_P–H···O=C, while for weak interactions such as C–H···O interactions, the dispersion contribution becomes a dominating factor; (c) the results obtained from PIXEL and AIM calculations show that the N_{CP}–H···O=P hydrogen bond has a higher strength than the N_P–H···O = C; (d) all obtained results give evidences for the importance of strong N–H···O interactions in molecular assemblies of phosphoric triamides, while, at the same time, the weaker interactions play a decisive role in the crystal packing.

Experimental

All chemicals were of analytical grade, obtained from commercial sources and used without purification. Infrared (IR) spectra were recorded on a Bruker ALPHA FT-IR spectrometer using a KBr disk. ^{1}H, ^{13}C, $^{31}P\{^{1}H\}$, and $^{19}F\{^{1}H\}$ NMR spectra were recorded on an FT-NMR Bruker Avance DRX 400 spectrometer, using TMS for ^{1}H and ^{13}C, 85% H_3PO_4 for ^{31}P, and CF_3Cl for ^{19}F (as internal standards).

Crystal structure determination

A suitable single crystal for each of the compounds **1**–**3** was selected for the X-ray diffraction experiment and mounted on a glass fiber.

For structures **1**–**3**, measurements were made on a Gemini diffractometer with graphite monochromated Mo $K\alpha$ radiation (λ = 0.7107 Å) and equipped with a Sapphire3 CCD detector. The data were corrected for absorption using redundant reflections with CrysAlisPro [26]. Structures were solved using the charge-flipping method implemented in the Superflip program [27] and refined using the CRYSTALS program [28]. Non-H atoms were refined anisotropically. After that, the H atoms were all located in the difference Fourier maps for each of structures, but those attached to C atoms were repositioned geometrically. The H atoms were initially refined with soft restraints on the bond lengths and angles to regularise their geometry (C–H in the range 0.93–0.98 Å and N–H in the range 0.86–0.89 Å), after which the positions were refined with riding constraints [29] and fixed isotropic displacement parameters $U_{iso}(H) = 1.5U_{eq}(C_i)$ for CH_3 groups or $1.2U_{eq}(C_{ii})$ for CH_2 and CH groups, where $U_{eq}(C_i)$ and $U_{eq}(C_{ii})$ are the equivalent displacement parameters of the C atoms to which corresponding H atoms are bonded.

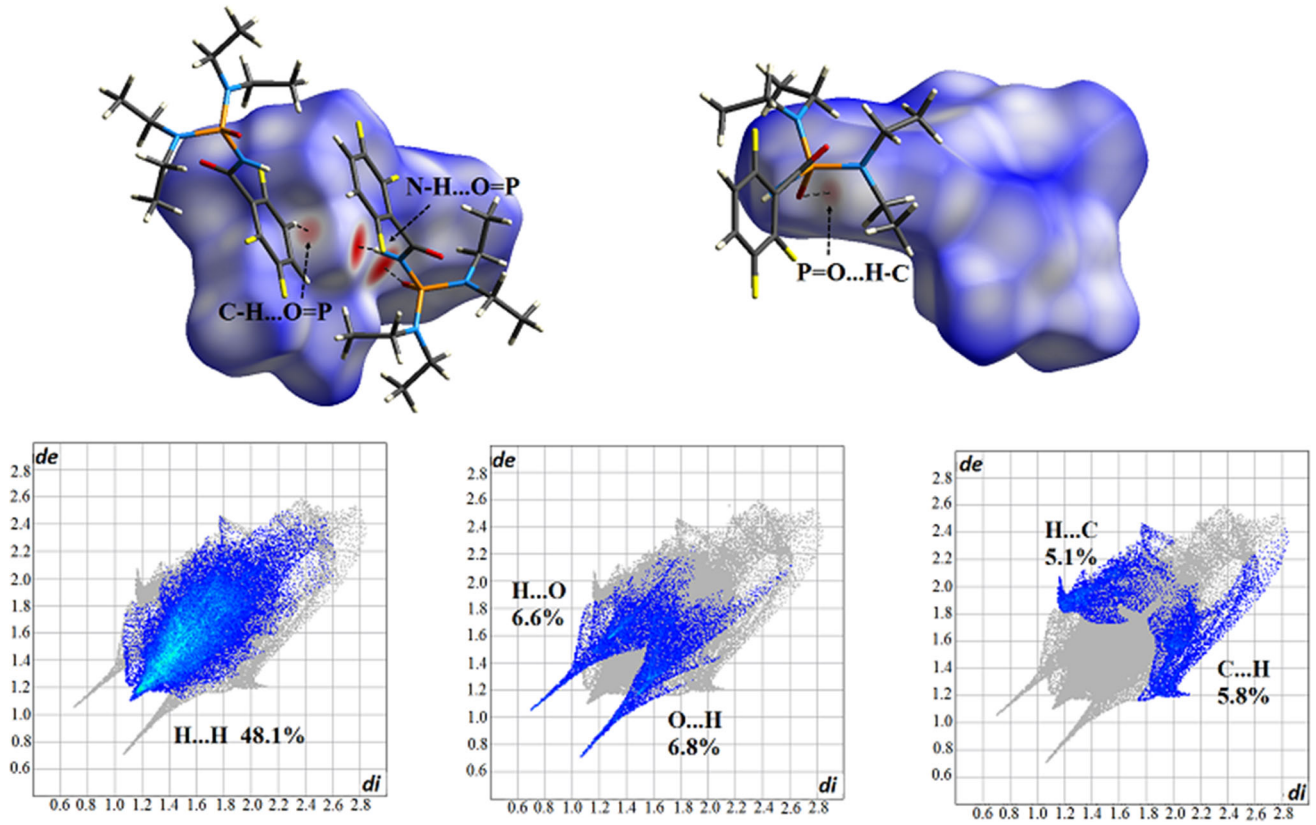

Fig. 10 Up: d_{norm} Hirshfeld surface surrounded by neighboring molecules associated with close contacts for molecule P1 of **2** in two different orientations. Down: decomposed fingerprint plots and percentage contributions to the total HS for intermolecular contacts H…H, O…H/H…O and C…H/H…C for molecule P1 of **2**. The full fingerprint plot appears as a grey shadow below each decomposed plot

CCDC numbers 1541709, 1541710 and 1541711 for three reported structures **1**–**3** contain the supplementary crystallographic data for this paper. These data can be obtained free of charge from Cambridge Crystallographic Data Centre via http://www.ccdc.cam.ac.uk/data_request/cif.

A Hirshfeld Atomic Refinement (HAR) was also performed for the two non-disordered structures. As can be seen from Table S1, the refinement are considerably improved, from R_1 = 0.0528 to R_1 = 0.0327 for structure **1**, and from R_1 = 0.0771 to R_1 = 0.0568 for structure **2**. The positional and anisotropic Atomic Displacement Parameters (ADP) of all hydrogen atoms were refined, giving realistic 'neutron' carbon and nitrogen to hydrogen distances. For **2**, the ADPs of the hydrogen atoms bounded to nitrogen appeared to be non-positive definite, showing still some shortcomings in either the data quality or the crystal-field-embedded quantum-chemical electron density. For structure, all H-atom ellipsoids are positive definite. The largest differences between the classical and Hirshfeld atomic refinement concern evidently the H-atom positions. For instance, the P1–N11–H111 angle in the classical structure **1** is 115.96° and that in the HAR structure 114.53°. The largest distance difference between the two structures is also for H111, i.e., 0.16 Å. For a very accurate description of the hydrogen-bond interactions in a structure, it is thus preferable to use a HAR. However, just because of the ADP's of the hydrogens involved in hydrogen-bond interactions in **2** are non-positive definite, we prefer to use the classical description for the discussion below. For the details of the HAR refinements, see the supplementary material of this paper (Table S1 and Figs. S4 and S5). The arithmetic mean of the distance between the two models for structure **1** is 0.0631 Å and that for structure **2** 0.0699 Å. The measures of similarity are 0.009 for both **1** and **2**. Without hydrogen atoms, the arithmetic means of the distance difference are 0.0044 Å and 0.0057 Å for **1** and **2**, respectively, and the similarity indices 0.001 for both **1** and **2**.

PLATON [30] and Mercury [31] programs were used for making the ORTEP and packing diagrams. COMPSTRU [32] was used for the structure similarity calculations.

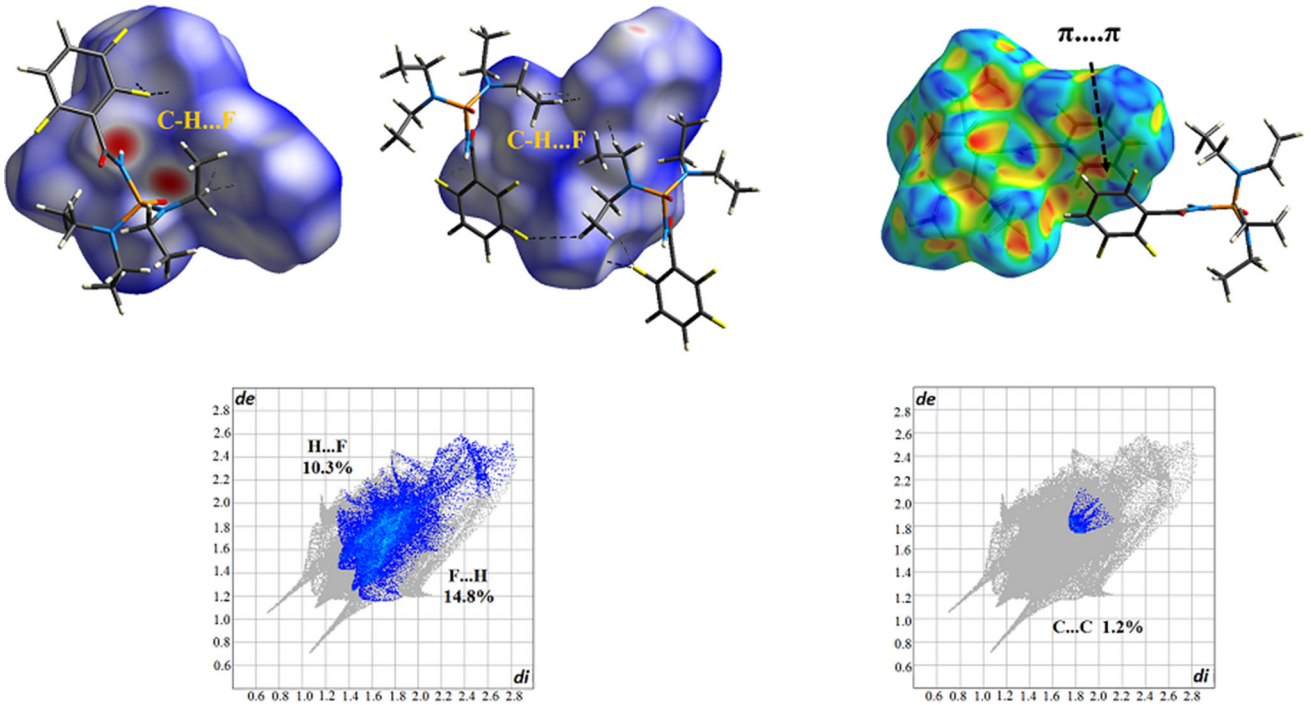

Fig. 11 Up: d_{norm} Hirshfeld surface in two different orientations (left and middle) and Hirshfeld surface mapped with shape index (right), surrounded by neighboring molecules associated with close contacts H…F/F…H (black dash lines, white areas) or π…π stacking, for molecule P1 of **2**. Down: Decomposed fingerprint plots and percentage contributions to the total HS for intermolecular contacts F…H/H…F and C…C for molecule P1 of **2**. The full fingerprint plot appears as a grey shadow below each decomposed plot

Synthesis of phosphoric triamides 1 and 2

2,3,6-F_3–$C_6H_2C(O)NHP(O)Cl_2$ was synthesized from the reaction of phosphorus pentachloride (16 mmol) and 2,3,6-trifluorobenzamide (16 mmol) in dry CCl_4 at 358 K (3 h) under reflux condition and then the treatment of formic acid (16 mmol) at ice bath temperature. For the preparation of **1**, a solution of 2,3,6-F_3–$C_6H_2C(O)NHP(O)Cl_2$ (2 mmol) in 20 cm^3 CH_3CN was added at 273 K to a solution of *N*-methylcyclohexylamine (8 mmol) in 5 cm^3 of the same solvent. After stirring for 4 h, the solvent was evaporated and the product was washed with distilled water. Compound **2** obtained in a similar procedure to **1** but using diethylamine instead of *N*-methylcyclohexylamine. Colorless single crystals, suitable for X-ray structural analysis, were obtained at room temperature from a mixture of CH_3OH/DMF/*n*-C_6H_{14} (3:1:1 v/v) for both **1** and **2**.

***N,N′*-Dicyclohexyl-*N″*-(2,3,6-trifluorobenzoyl)-*N,N′*-dimethylphosphoric triamide (1, $C_{21}H_{31}F_3N_3O_2P$)** Mp.: 172 °C; IR (KBr): $\bar{\nu}$ = 3047, 2935, 2858, 2781, 1670, 1636, 1491, 1456, 1296, 1221, 1180, 1061, 1024, 972, 951, 827, 720, 771, 571, 507, 468 cm^{-1}; ^1H NMR (400.13 MHz, DMSO-d_6, 297.5 K, TMS): δ = 0.99–1.77 (m, 20H), 2.54 (m, 6H), 3.33 (m, 2H), 7.21 (m, 1H, Ar–H), 7.59 (m, 1H, Ar–H), 8.28 (s, 1H, NH) ppm; ^{13}C NMR (100.62 MHz, DMSO-d_6, 298.4 K, TMS): δ = 24.33 (s, 2C), 25.57 (s, 2C), 27.71 (d, ^3J(P,C) = 4.6 Hz, 2C), 30.76 (m, 6C), 54.72 (d, ^2J(P,C) = 4.6 Hz, 2C), 112.55 (d, ^2J(F,C) = 21.3 Hz, 1C, C_{Ar}), 117.71 (m, 1C, C_{Ar}), 118.89 (m, 1C, C_{Ar}), 145.30 (m, 1C, C_{Ar}), 147.74 (m, 1C, C_{Ar}), 154.31 (d, ^1J(F,C) = 249.7 Hz, 1C, C_{Ar}), 160.81 (s, 1C, C(O)) ppm; $^{31}P\{^1H\}$ NMR (161.97 MHz, DMSO-d_6, 298.4 K, 85% H_3PO_4): δ = 11.69 (s) ppm; ^{19}F NMR (376.47 MHz, DMSO-d_6, 296.5 K, $CFCl_3$): δ = − 142.53 (s), − 138.16 (m), − 119.25 (m) ppm.

***N,N,N′,N′*-Tetraethyl-*N″*-(2,3,6-trifluorobenzoyl)phosphoric triamide (2, $C_{15}H_{23}F_3N_3O_2P$)** Mp.: 126 °C; IR (KBr): $\bar{\nu}$ = 3061, 2976, 2935, 2876, 1695, 1633, 1492, 1473, 1385, 1282, 1217, 1175, 1105, 1022, 947, 849, 829, 795, 719, 641, 623, 559, 498 cm^{-1}; ^1H NMR (400.13 MHz, DMSO-d_6, 295.8 K, TMS): δ = 1.06 (t, ^3J(H,H) = 7.1 Hz, 12H, $4CH_3$), 2.50–3.34 (m, 8H, $4CH_2$), 7.21 (m, 1H, Ar–H), 7.59 (m, 1H, Ar–H), 9.77 (s, 1H, NH) ppm; ^{13}C NMR (100.62 MHz, DMSO-d_6, 298.5 K, TMS): δ = 14.17 (d, ^3J(P,C) = 1.9 Hz, 4C), 39.13 (d, ^2J(P,C) = 4.8 Hz, 4C), 112.53 (d, ^2J(F,C) = 24.3 Hz, 1C, C_{Ar}), 117.72 (m, 1C, C_{Ar}), 118.91 (m, 1C, C_{Ar}), 145.37 (m, 1C, C_{Ar}), 147.82 (m, 1C, C_{Ar}), 154.34 (d, ^1J(F,C) = 245.8 Hz, 1C, C_{Ar}), 160.81 (s, 1C, C(O)) ppm; $^{31}P\{^1H\}$ NMR (161.97 MHz, DMSO-d_6, 296.4 K, 85% H_3PO_4): δ = 10.76 (s) ppm; ^{19}F NMR (376.47 MHz, DMSO-d_6, 295.5 K, $CFCl_3$): δ = − 142.57 (s), − 138.01 (m), − 119.00 (m) ppm.

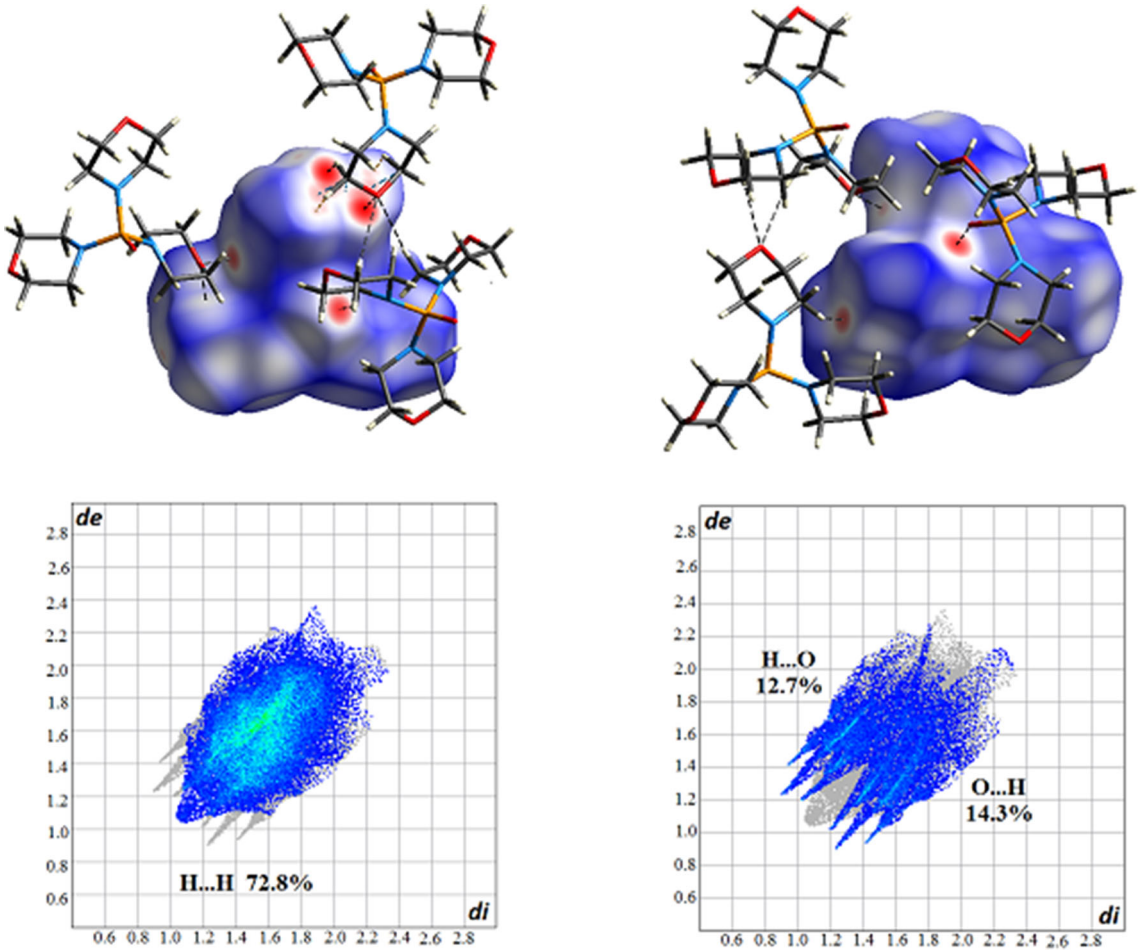

Fig. 12 Up: views of d_{norm} Hirshfeld surface for **3** generated for the major disordered components in two orientations, surrounded by neighboring molecules associated with close contacts O…H/H…O (C–H…O hydrogen bonds, black dashed lines) as red spots on surface; down: decomposed H…H and O…H/H…O FPs and related percentage contribution to the total HS area shown in down

Tris(morpholin-4-yl) phosphine oxide (3) For the preparation of **3**, a solution of morpholine (12 mmol) in 5 cm^3 dry CH_3CN was added at 273 K to a solution of $P(O)Cl_3$ (2 mmol) in 10 cm^3 of the same solvent. After stirring for 4 h, the precipitated amine hydrochloride salt ($OC_4H_8NH{\cdot}HCl$) was filtered off and the acetonitrile solution of $[OH_8C_4N]_3P(O)$ was used in a reaction with $Cu(NO_3)_2{\cdot}4H_2O$ in CH_3OH under reflux. Single crystals of **3** were obtained fortuitously from slow evaporation of the filtered solution of the mentioned reaction at room temperature. M.p.: 184–186 °C (187–188 °C [19]); IR (KBr): $\bar{\nu}$ = 2965, 2847, 1456, 1367, 1325, 1296, 1258, 1207, 1130, 1115, 1090, 1024, 956, 918, 847, 733, 675, 621, 571, 518, 482 cm^{-1}.

Computational calculations

Optimization of the crystal structures was performed at MP2 level of theory at 6-31G(d,p) basis set using Gaussian09 [33]. The structures for the studied molecules were fully optimized and characterized as true minima by the absence of imaginary frequencies, but the calculations for the analysis of the crystal structure and intermolecular interactions were performed using the crystal geometry, i.e., with possible imaginary frequencies. The C–H-bond lengths were renormalized to their neutron value of 1.08 Å, while O–H and N–H bonds were fixed at 1.00 Å. Lattice and intermolecular interaction energies were calculated using the PIXEL module in the Coulomb London Pauli (CLP) computer program package [34]. The program PIXEL provides the advantage of partitioning the total interaction energy for the different molecular pairs into the corresponding coulombic, polarization, dispersion, and repulsion components, respectively, which reveals how molecules interact in crystals. Coulombic and linear-polarization terms are calculated by classical formulae [35] using charge densities and their electric fields, whereas the dispersion and repulsion terms are evaluated by the London approach [36] and Pauli spin avoidance [37], respectively, where the former term is due to electron correlation and the

latter term is appraised depending on the amount of overlap between proximal charge densities [17]. Selected molecular pairs were further analyzed using the Atom In Molecule (AIM) theory (at the MP2/6-31G(d,p) level) which is a method providing a vigorous and unambiguous criterion to determine which atoms are bonded and which atoms are separated in the system [38]. In this method, the topological properties of charge density ($\vec{\rho}_r$) and the Laplacian of the electronic charge density ($\nabla^2\vec{\rho}_r$) are of interest which summarized by their critical points (CPs).

Hirshfeld surface analysis

To manifest the molecular assemblies via weak intermolecular interactions in **1**–**3**, 3D Hirshfeld surfaces (HSs) and 2D fingerprint plots (FPs) are generated using CrystalExplorer17 [39]. The bond lengths to hydrogen were set to standard (neutron) values (C–H = 1.083 Å and N–H = 1.009 Å) during the calculations. Close intermolecular interactions identified as red spots on the d_{norm} HSs in Figs. 8, 9, 10, 11, 12, and S1–S3 are listed in Table 3. For **3**, because of the disorder present, the HS analysis was performed for the two possible orientations separately.

The generated Hirshfeld surfaces are mapped over d_{norm} and the shape index. The d_{norm} surface is the normalized function of d_{i} and d_{e} (the distances from a point on the surface to the nearest atom interior and exterior to the surface, respectively) as $d_{\text{norm}} = \frac{d_i - r_i^{\text{vdw}}}{r_i^{\text{vdw}}} + \frac{d_e - r_e^{\text{vdw}}}{r_e^{\text{vdw}}}$ with white-, red-, and blue-colored surfaces. The white surface indicates those contacts with distances equal to the sum of the van der Waals (vdW) radii, and red and blue surfaces indicate contacts shorter and longer than sum of vdW radii, respectively [40].

The HS fingerprint plots (FPs) [41, 42] can be used to decompose the contribution of intermolecular interactions in the construction of the 3D architecture. These plots quantitatively summarize the information provided by the generated HSs in a 2D grid histogram constructed from the pair distance d_{e}, d_{i} for each individual surface spot. The frequency of occurrence of any given pair of d_{e}, d_{i} is represented by the blue-green–red color feature as low-, medium-, and high-frequent occurrence, respectively [14]. Moreover, the "decomposed" FPs, which show the isolation of any given interaction with a color scheme only to relevant interactions, include the reciprocal X···H/H···X contacts, X is located inside (for X···H/$d_{\text{e}} < d_{\text{i}}$) or outside (for H···X/$d_{\text{e}} > d_{\text{i}}$) the generated HS as an H-atom acceptor. The complementary regions, where one molecule is a donor ($d_{\text{e}} > d_{\text{i}}$) and the other as an acceptor ($d_{\text{e}} < d_{\text{i}}$), can be also identified in the FPs [43].

Acknowledgements Support of this investigation by Semnan University is gratefully acknowledged.

References

1. Hoon Kwon C, Young Moon K, Baturay N, Shirota FN (1991) J Med Chem 34:588
2. Jain M, Fan J, Baturay NZ, Kwon C-H (2004) J Med Chem 47:3843
3. Hu L, Yu C, Jiang Y, Han J, Li Z, Browne P, Race PR, Knox RJ, Searle PF, Hyde EI (2003) J Med Chem 46:4818
4. Quintero L, Sánchez-Vazquez M, Cruz-Gregorio S, Sartillo-Piscil F (2010) J Org Chem 75:5852
5. Font M, Domínguez M-J, Sanmartín C, Palop JA, San-Francisco S, Urrutia O, Houdusse F, García-Mina JM (2008) J Agric Food Chem 56:8451
6. Domínguez MJ, Sanmartín C, Font M, Palop JA, San Francisco S, Urrutia O, Houdusse F, García-Mina JM (2008) J Agric Food Chem 56:3721
7. Nakashima D, Yamamoto H (2006) J Am Chem Soc 128:9626
8. Nishikawa Y, Nakano S, Tahira Y, Terazawa K, Yamazaki K, Kitamura CH, Hara O (2016) Org Lett 18:2004
9. Pourayoubi M, Toghraee M, Zhu J, Dušek M, Bereciartua PJ, Eigner V (2014) CrystEngComm 16:10870
10. Palatinus L, Brázda P, Boullay P, Perez O, Klementová M, Petit S, Eigner V, Zaarour M, Mintova S (2017) Science 355:166
11. Capelli SC, Bürgi H-B, Dittrich B, Grabowsky S, Jayatilaka D (2014) IUCrJ 1:361
12. Woińska M, Grabowsky S, Dominiak PM, Woźniak K, Jayatilaka D (2016) Sci Adv 2:e1600192
13. McKinnon JJ, Mitchell AS, Spackman MA (1998) Chem Eur J 4:2136
14. Spackman MA, McKinnon JJ (2002) CrystEngComm 4:378
15. Dunitz JD, Gavezzotti A, Rizzato S (2014) Cryst Growth Des 14:357
16. Shukla R, Shripanavar C, Chopra D, Bubbly SG, Gudennavar SB (2015) Struct Chem Cryst Comm 1:1
17. Gavezzotti A (2011) New J Chem 35:1360
18. Pourayoubi M, Tarahhomi A, Rheingold AL, Golen JA (2010) Acta Cryst E66:o3159
19. Romming C, Songstad J (1982) Acta Chem Scand A 36:665
20. Tarahhomi A, Pourayoubi M, Golen JA, Zargaran P, Elahi B, Rheingold AL, Leyva Ramírez MA, Mancilla Percino T (2013) Acta Cryst B69:260
21. Tarahhomi A, Pourayoubi M, Rheingold AL, Golen JA (2011) Struct Chem 22:201
22. Pourayoubi M, Tarahhomi A, Saneei A, Rheingold AL, Golen JA (2011) Acta Cryst C67:o265
23. Pourayoubi M, Toghraee M, Divjakovic V, van der Lee A, Mancilla Percino T, Leyva Ramírez MA, Saneei A (2013) Acta Cryst B69:184
24. Mazur L, Koziol AE, Jarzembska KN, Paprocka R, Modzelewska-Banachiewicz B (2017) Cryst Growth Des 17:2104
25. Martin AD, Britton J, Easun TL, Blake AJ, Lewis W, Schröder M (2015) Cryst Growth Des 15:1697
26. Agilent CrysAlis PRO (2011) Agilent technologies. Yarnton, Oxfordshire
27. Palatinus L, Chapuis G (2007) J Appl Cryst 40:786
28. Betteridge PW, Carruthers JR, Cooper RI, Prout K, Watkin DJ (2003) J Appl Cryst 36:1487
29. Cooper RI, Thompson AL, Watkin DJ (2010) J Appl Cryst 43:1100
30. Spek AL (2009) Acta Cryst D65:148

31. Macrae CF, Bruno IJ, Chisholm JA, Edgington PR, McCabe P, Pidcock E, Rodriguez-Monge L, Taylor R, van de Streek J, Wood PA (2008) J Appl Cryst 41:466
32. de la Flor G, Orobengoa D, Tasci E, Perez-Mato JM, Aroyo MI (2016) J Appl Cryst 49:653
33. Frisch MJ, Trucks GW, Schlegel HB, Scuseria GE, Robb MA, Cheeseman JR, Montgomery Jr JA, Vreven T, Kudin KN, Burant JC, Millam JM, Iyengar SS, Tomasi J, Barone V, Mennucci B, Cossi M, Scalmani G, Rega N, Petersson GA, Nakatsuji H, Hada M, Ehara M, Toyota K, Fukuda R, Hasegawa J, Ishida M, Nakajima T, Honda Y, Kitao O, Nakai H, Klene M, Li X, Knox JE, Hratchian HP, Cross JB, Adamo C, Jaramillo J, Gomperts R, Stratmann RE, Yazyev O, Austin AJ, Cammi R, Pomelli C, Ochterski JW, Ayala PY, Morokuma K, Voth GA, Salvador P, Dannenberg JJ, Zakrzewski VG, Dapprich S, Daniels AD, Strain MC, Farkas O, Malick DK, Rabuck AD, Raghavachari K, Foresman JB, Ortiz JV, Cui Q, Baboul AG, Clifford S, Cioslowski J, Stefanov BB, Liu G, Liashenko A, Piskorz P, Komaromi I, Martin RL, Fox DJ, Keith T, Al-Laham MA, Peng CY, Nanayakkara A, Challacombe M, Gill PMW, Johnson B, Chen W, Wong MW, Gonzalez C, Pople JA (2009) Gaussian 09, Revision B.04. Gaussian, Inc, Pittsburgh, PA
34. Dunitz JD, Gavezzotti A (2012) Cryst Growth Des 12:5873
35. Feynman RP (1989) The Feynman lectures on physics, vol 2. Addison-Wesley, Reading
36. London F (1937) Trans Faraday Soc 33:8
37. Kauzmann W (1957) Quantum chemistry, an introduction. Academic Press, New York, p 305
38. Bader RFW (1990) Atoms in molecules, a quantum theory. Oxford University Press, New York
39. Turner MJ, McKinnon JJ, Wolff SK, Grimwood DJ, Spackman PR, Jayatilaka D, Spackman MA (2017) CrystalExplorer17. University of Western Australia
40. McKinnon JJ, Spackman MA, Mitchell AS (2004) Acta Cryst B60:627
41. McKinnon JJ, Jayatilaka D, Spackman MA (2007) Chem Commun 3814
42. Spackman MA, Jayatilaka D (2009) Cryst EngComm 11:19
43. Fabbiani FPA, Leech CK, Shankland K, Johnston A, Fernandes P, Florence AJ, Shankland N (2007) Acta Cryst C63:o659